PNAS RESEARCH ARTICLE | PHYSICS OPEN ACCESS

Self-propelling colloids with finite state dynamics

Steven van Kesteren[a], Laura Alvarez[a,b], Silvia Arrese-Igor[c], Angel Alegria[c], and Lucio Isa[a,1]

Edited by Ramin Golestanian, Max-Planck-Institut for Dynamik and Selbstorganisation, Göttingen, Germany; received August 14, 2022; accepted January 28, 2023, by Editorial Board Member Paul Chaikin

Endowing materials with the ability to sense, adapt, and respond to stimuli holds the key to a progress leap in autonomous systems. In spite of the growing success of macroscopic soft robotic devices, transferring these concepts to the microscale presents several challenges connected to the lack of suitable fabrication and design techniques and of internal response schemes that connect the materials' properties to the function of the active units. Here, we realize self-propelling colloidal clusters which possess a finite number of internal states, which define their motility and which are connected by reversible transitions. We produce these units via capillary assembly combining hard polystyrene colloids with two different types of thermoresponsive microgels. The clusters, actuated by spatially uniform AC electric fields, adapt their shape and dielectric properties, and consequently their propulsion, via reversible temperature-induced transitions controlled by light. The different transition temperatures for the two microgels enable three distinct dynamical states corresponding to three illumination intensity levels. The sequential reconfiguration of the microgels affects the velocity and shape of the active trajectories according to a pathway defined by tailoring the clusters' geometry during assembly. The demonstration of these simple systems indicates an exciting route toward building more complex units with broader reconfiguration schemes and multiple responses as a step forward in the pursuit of adaptive autonomous systems at the colloidal scale.

active matter | microrobotics | microswimmers

Significance

The miniaturization of autonomous systems down to the colloidal scale requires transferring functions, such as sensing or reconfiguration, to the constituent materials. Currently, limitations in fabrication and control strategies remain prevalent. Here, we combine directed particle assembly via capillary forces with multiple thermoresponsive microscale hydrogels to realize colloidal clusters that can self-propel under AC electric fields and that explore multiple dynamical states via well-defined temperature-induced transitions controlled by light. These simple, multistate active units constitute a promising step toward advancing our capabilities to fabricate small-scale adaptive agents, inspired by larger-scale soft robotic systems, in a conceivably not-too-distant future.

As automation increasingly pervades our lives, new paradigms for autonomous systems across a broad range of length scales and application fields are in high demand. The recent upsurge of soft robotics is a clear example, where strong efforts are currently underway to endow robots with so-called physical intelligence (1). This concept aims at transferring functions, including sensing, actuation, and adaptation to the materials that these active units are made of (2). A key trait of autonomous systems is their ability to move in the presence of an onboard energy source or by harvesting available "fuel," which can be both of chemical origin or an external field, e.g., acoustic, thermal, or electromagnetic. A conceptually straightforward way to develop adaptive motion is to select propulsion or actuation strategies that depend on the state of a material, e.g., solid/liquid, expanded/contracted, soft/stiff, conductive/nonconductive, etc., which can be switched by a specific trigger, such as temperature, light, or chemical signals. By selecting materials with multiple internal states and/or by combining them, one can then achieve systems with a finite number of dynamical states, as, for instance, shown for macroscopic systems (3–5) or active droplets (6, 7).

However, the extension of these concepts to the (sub)micrometric or colloidal scale still presents significant challenges. Self-propelling particles, aka artificial microswimmers or active colloids, are at the core of current and future applications to act as delivery vehicles (8–11), active mixers (12), or remediation agents (13, 14), to name a few. Crucially, the self-propulsion of active colloids is enabled by their intrinsic geometrical or compositional asymmetry, which defines the magnitude and directionality of their motion (15). However, this asymmetry is typically fixed during synthesis and fabrication (16, 17), implying that synthetic colloidal microswimmers only have one internal dynamical state and that propulsion is regulated by controlling the energy input.

Endowing active particles with adaptive, multistate dynamics requires the following features: i) a self-propulsion mechanism that depends on the particle's state, i.e., shape or internal properties; ii) the possibility to encode the states and their transitions in a deterministic fashion during fabrication; and iii) the possibility to reversibly switch between different states in response to well-defined inputs.

In this work, we fulfill these three requirements by fabricating artificial microswimmers constituted by colloidal clusters or "molecules" (18–20), which combine responsive and nonresponsive particles (21). The clusters are deterministically prepared by means

Author contributions: L.I. designed research; S.v.K., L.A., S.A.-I., A.A., and L.I. performed research; S.v.K., L.A., S.A.-I., A.A., and L.I. analyzed data; and S.v.K., L.A., and L.I. wrote the paper.

The authors declare no competing interest.

This article is a PNAS Direct Submission. R.G. is a guest editor invited by the Editorial Board.

[1]To whom correspondence may be addressed. Email: lucio.isa@mat.ethz.ch.

This article contains supporting information online at http://www.pnas.org/lookup/suppl/doi:10.1073/pnas.2213481120/-/DCSupplemental.

Published March 7, 2023.

of sequential capillarity-assisted particle assembly (or sCAPA) (22). They furthermore exhibit self-propulsion under spatially uniform AC electric fields in the kHz region, which are applied perpendicularly to the electrodes over which the particles move thanks to asymmetric electrohydrodynamic flows (EHDFs) (23–26). The transition between the different dynamical states is triggered by externally imposed temperature signals, which cause the reconfiguration of the shape and dielectric properties of the clusters. We first begin by conceptually describing our approach to achieve microswimmers with multistate dynamics and then focus on their experimental realization and characterization.

Self-Propelling Colloids with Finite State Dynamics: The Concept. The conceptually simplest case of a self-propelling particle with multiple dynamical states is a two-state particle. Given the requirement for asymmetry, a two-state active particle can be realized by constructing a dumbbell where one of the two lobes changes its properties in response to an input signal.

By selecting EHDF-induced propulsion and temperature signals, dumbbells comprising one nonresponsive, e.g., polystyrene (PS), lobe and one responsive, e.g., poly(N-isopropylacrylamide)-based, lobe fulfill the criteria. Poly(N-isopropylacrylamide) (PNIPAM) is a thermoresponsive polymer that undergoes a reversible lower critical solubility transition at a well-defined temperature. PNIPAM-based particles (or microgels) correspondingly undergo a swelling/deswelling transition at that temperature, called the volume phase transition temperature or VPTT. Upon crossing the VPTT, microgels experience a volumetric change coupled to a variation of their dielectric properties (21, 27–29). Self-propulsion of dumbbells generated by EHDFs depends both on the relative dimensions of the two lobes and on their dielectric properties (16, 24). The existence of two different dynamical states for reconfigurable, PNIPAM-based active dumbbells has in fact been recently demonstrated (21).

However, the VPTT of the microgels depends on their chemistry, their internal architecture, e.g., crosslinking density (30), and the solvent properties (31). In this work, we synthesize and use two types of thermoresponsive PNIPAM-based microgels to enable the access of multiple dynamical states (*Methods*). In particular, we use two different comonomers, methacrylic acid (MAA) and acrylic acid (AA), in the polymerization of PNIPAM to obtain microgels with different VPTTs. The PNIPAM-co-MAA microgels have a green-fluorescent (BODIPY) core and the PNIPAM-co-AA microgels have a red-fluorescent (Nile-red) core and are henceforth termed green (G) and red (R) microgels. Due to the higher hydrophilicity of AA compared to MAA, its VPTT is shifted to higher temperatures (32–34). The VPTT of green-core microgels is $T_{G \rightleftharpoons G'} \approx 29$ °C and one of the red-core microgels is $T_{R \rightleftharpoons R'} \approx 33$ °C (*SI Appendix*, section 1 for further details).

By using these microgels, we can therefore construct two different types of dumbbells, G-PS and R-PS, respectively, of which we can schematically represent the different states and their transitions, as shown in Fig. 1*A*. The G-PS dumbbells undergo a transition between a swollen state G to a collapsed state G' ($G \rightleftharpoons G'$) at a temperature $T_{G \rightleftharpoons G'}$ and correspondingly the transition $R \rightleftharpoons R'$ takes place at $T_{R \rightleftharpoons R'}$. As it will be shown below, these two transitions correspond to a switch between two different self-propulsion modes, with an adaptation of the propulsion velocity $V_G \rightleftharpoons V_{G'}$ and $V_R \rightleftharpoons V_{R'}$, respectively.

The existence of two different transition temperatures opens the way to the fabrication of microswimmers with three distinct dynamical states by incorporating both G and R microgels in a colloidal trimer together with a PS particle, as schematically shown in Fig. 1*B*. Upon crossing $T_{G \rightleftharpoons G'}$, the trimer goes from a fully swollen state to one where only the G microgel is collapsed $GR \rightleftharpoons G'R$; when $T_{R \rightleftharpoons R'}$ is crossed, both microgels shrink and the trimer undergoes the $G'R \rightleftharpoons G'R'$ transition. The order of the transitions is reversed by progressively reducing temperature. Using two different microgels, which can have different sizes and dielectric properties in both the swollen and collapsed state, can cause the breaking of the axial symmetry of the trimer. Sequential swelling and deswelling of the particles can thus lead to state-dependent chiral trajectories, in addition to three distinct translational velocities $V_{GR} \rightleftharpoons V_{G'R} \rightleftharpoons V_{G'R'}$. We remark that nonchiral trajectories can be in principle encoded by design,

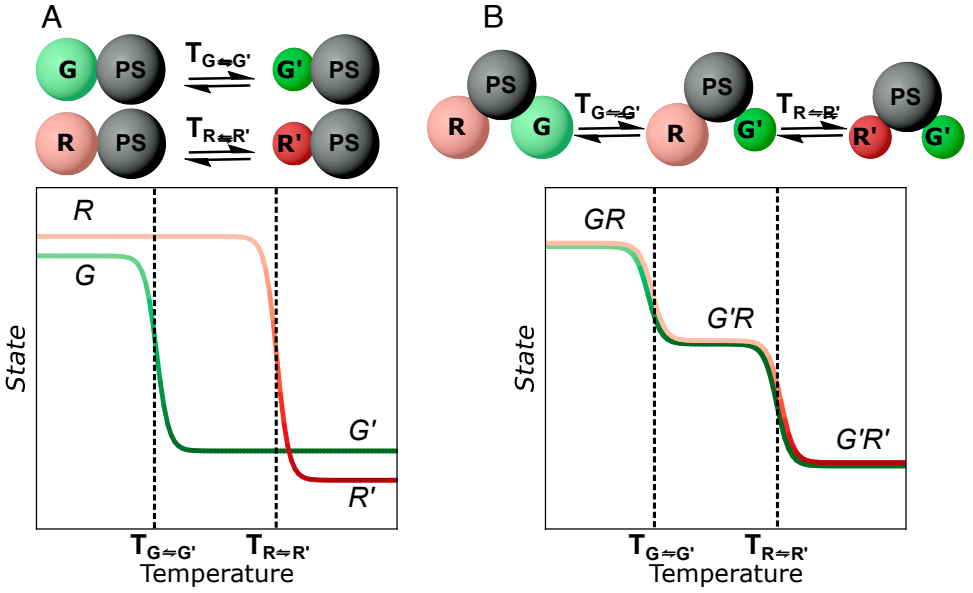

Fig. 1. Schematic representation of the multistate dynamics of reconfigurable colloidal clusters. (*A*) Representation of the reconfiguration of G-PS and R-PS dumbbells upon crossing the respective transition temperatures $T_{G \rightleftharpoons G'}$ and $T_{R \rightleftharpoons R'}$ and schematic of the corresponding transition between the different states as a function of temperature T. (*B*) Extension of the previous concept to a three-state particle (R-G-PS trimer).

but their practical implementation presents some difficulties, as described later.

Two-State Dynamics: Self-Propelling Responsive Dumbbells. After introducing the concept in the previous Section, we now show that the behavior schematically displayed in Fig. 1*A* can be experimentally implemented. We synthesized PNIPAM-co-MAA (G) microgels and PNIPAM-co-AA (R) microgels that have a hydrodynamic diameter of ≈ 2-3 μm before and ≈ 0.7–1.2 μm after their respective VPPT (*SI Appendix*, Fig. S4). In both cases, the fluorescent cores are made from poly 2-trifluoromethylacrylic (PTFMA) and have a diameter of around 200 nm, to visualize the different microgels under the microscope. The G-PS and R-PS dumbbells are obtained using sCAPA, as previously described (21, 22). In short, both PS particles and microgels are sequentially deposited into predesigned traps microfabricated on a polydimethylsiloxane (PDMS) template. An evaporating droplet of the target particle suspension is moved over the PDMS template at a controlled speed and capillary forces selectively place the particles inside the traps. PS particles are deposited first, followed by either the G or R microgels to obtain the dumbbells inside the traps (Fig. 2 *A* and *B*). After deposition, the particles are linked by thermal sintering at 75 °C for 15 min and harvested using an adhesive sacrificial layer of glucose.

The resulting dumbbells are dispersed in a dilute HEPES buffer and confined between two transparent electrodes consisting of glass slides coated by a Cr and a Au layer covered with a polyethylene glycol (PEG) brush (*Methods*). The electrodes are separated by a 240-μm spacer and connected to a function generator that applies an AC electric field of 7 V peak-peak amplitude (300 V cm^{-1}) and 800 Hz frequency perpendicular to the electrodes. Upon application of the AC field, both the electrodes and the particles polarize; the presence of the particles close to the bottom electrode (where they sediment) causes a local distortion of the electric field generating a component that is tangential to the substrate, which in turn leads to the recirculation of ions, the so-called electrohydrodynamic flows (EHDFs), around each colloid (23). At a fixed voltage and frequency, the magnitude of the EHDFs depends on the particle size and dielectric properties (16, 23, 24). However, for homogeneous spherical particles, the EHDFs are radially symmetric and do not induce any net propulsion. Conversely, for dumbbells with lobes of different sizes and dielectric properties, the symmetry of the EHDFs is broken and a net fluid flow is generated, which leads to self-propulsion. In particular, if U_i is the magnitude of the velocity of the EHDF generated around particle i, the propulsion velocity of the dumbbell can be written, in first approximation, as $v_{ij} = (U_i r_j + U_j r_i)/(r_i + r_j)$, where r_i is the radius of particle i (or j, respectively), and $U_{i,j}$ is calculated at position $r_i + r_j$. The sign of the velocity U is defined as negative for attractive and positive for repulsive flows (24). Given that both U_{PS} and r_{PS} do not strongly depend on temperature, a sudden change in propulsion velocity is expected upon crossing $T_{G \rightleftharpoons G'}$ and $T_{R \rightleftharpoons R'}$ for the G-PS and R-PS dumbbells, respectively, because both the size and the dielectric properties of the microgels switch between different states upon crossing their respective VPTT (*SI Appendix*, section 2 for further details).

Experimentally, we induce controlled and rapid temperature variations by exploiting the plasmonic heating of the Au layer within the electrode upon illumination at 395 nm and 555 nm (35). By adjusting the light intensity, we can locally heat the system above $T_{G \rightleftharpoons G'}$ or $T_{R \rightleftharpoons R'}$ and correspondingly reconfigure the dumbbells (Fig. 2 *A* and *B* and *SI Appendix*, section 3 for further details of the experimental calibration and a numerical verification of the heating via finite element modelling (FEM) with COMSOL Multiphysics (36)). The system equilibrates within seconds and cools down upon removal of the illumination to ensure the reversible transition between the different states.

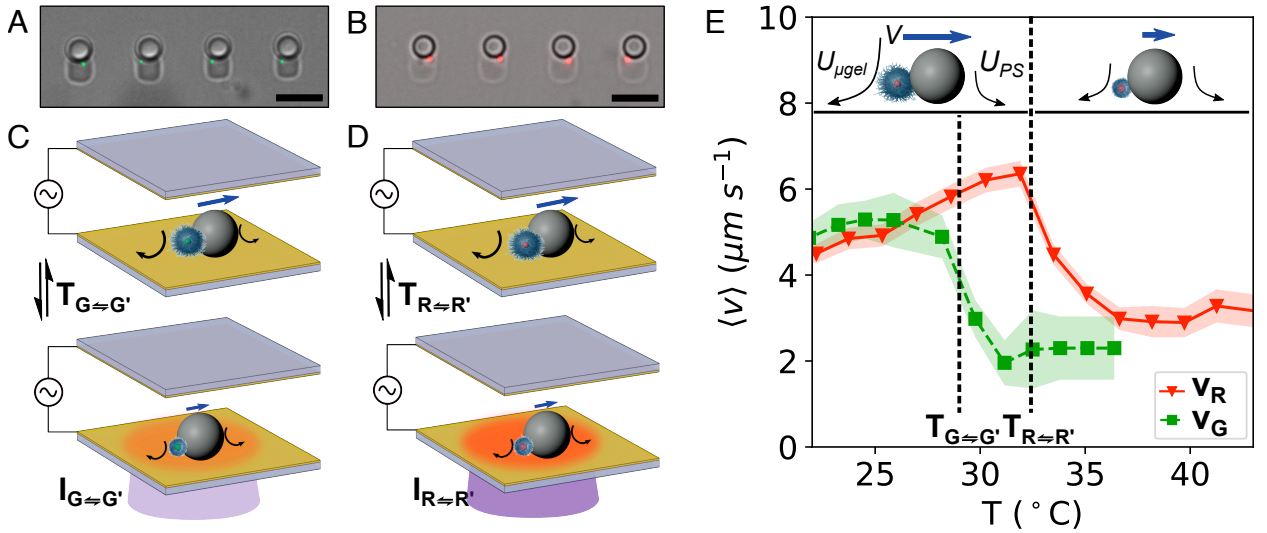

Fig. 2. Two-state microswimmers. (*A* and *B*) Combined bright-field+fluorescence micrographs of G-PS (*A*) and R-PS (*B*) dumbbells in the sCAPA traps. The scale bars are 5 μm. (*C* and *D*) Schematic of the experiment for the two-state temperature-induced switching in the self-propulsion of G-PS (*C*) and R-PS (*D*) dumbbells. The curved black arrows schematically represent the EHDFs generated by the PS and microgel lobes, respectively, and the straight blue arrows indicate the net propulsion due to these EHDFs. Plasmonic heating of the substrate illuminated with a light of intensity $I_{G \rightleftharpoons G'}$ ($I_{R \rightleftharpoons R'}$) raises the local temperature above $T_{G \rightleftharpoons G'}$ ($T_{R \rightleftharpoons R'}$) inducing a phase transition in the microgels. Note that because $T_{R \rightleftharpoons R'} > T_{G \rightleftharpoons G'}$, the corresponding illumination intensity is higher. (*E*) Mean self-propulsion velocity $< v >$ as a function of temperature T for the R-PS (triangles) and G-PS (squares) dumbbells. The shaded bands are the 99% confidence intervals calculated over 350 and 70 particles for the R-PS and G-PS, respectively. The vertical dashed lines mark the transition temperatures for the green and red core microgels, respectively. The inset schematically shows the switching of the self-propulsion state upon crossing the critical temperature, taking an R-PS dumbbell as an example. The black curved arrows represent the EHDFs generated by the microgel and the PS particle, with characteristic velocities U_{gel} and U_{PS}, respectively, and the straight blue arrows indicate the net propulsion with velocity V.

In line with previous observations (21), the collapse of the microgels significantly reduces the magnitude of the propulsion velocity of the microgel-PS dumbbells (Fig. 2*C*). In particular, $T_{G \rightleftharpoons G'}$ or $T_{R \rightleftharpoons R'}$ are sufficiently separated so that G microgels collapse while R ones are still in the swollen state, resulting in reconfiguration and velocity changes at distinct temperatures. This response follows the scheme proposed in Fig. 1*A* and holds the key to accessing additional dynamical states when combining both microgels in one active cluster.

Assembly of Multimicrogel Colloidal Clusters. The realization of the system proposed in Fig. 1*B*, implies achieving deterministic control on the relative position of the two microgels in the active G-R-PS trimer. As it can be seen in Fig. 2 *A* and *B*, conventional sCAPA in rectangular traps does not have sufficient positional control for the microgels, which are deposited on either side of the PS particles. In order to overcome this limitation, we have recently demonstrated a further refinement of sCAPA that exploits traps with three-dimensional height profiles realized by direct writing using a two-photon nanolithography system (Nanoscribe GT2 Professional), as schematically shown in Fig. 3*A* (*Methods* and *SI Appendix*, section 4 for further details) (37). We use the different heights of the different sections of the trap to guide the deposition of the PS particles and the R and G microgels into trimers with well-defined opening angles. The assembly process requires careful tuning of the trap geometry as well as of the deposition medium, speed, direction, and order (38). In particular, the PS particles are deposited first, followed by the R, and then the G microgels (Fig. 3*A*). The R microgels are selectively deposited in the deeper arm of the traps by using a lower surfactant concentration that gives a larger contact angle of the moving meniscus, decreasing the perpendicular capillary force to the plane that pushes the particles into the shallower arm of the traps. The G microgels are then deposited using a higher surfactant concentration, leading to a smaller contact angle of the droplet and higher perpendicular capillary forces that can confine them into the shallower arms, while the deeper ones are already occupied by the R microgels. By changing the geometry of the traps, we produced three-particle clusters with opening angles of 60, 120, and 180. We refer to these systems as 60-, 120-, or 180-clusters, and examples are shown in Fig. 3 *B*–*D*. The deposition yields go up to 75% for the 120-clusters (*SI Appendix*, section 5 for further details) and we use the same linking and harvesting procedures as for the dumbbells.

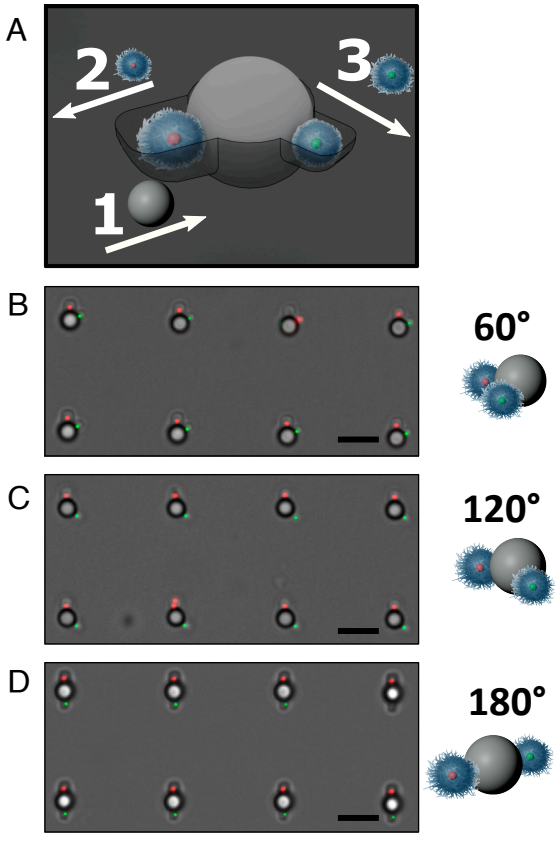

Fig. 3. Assembly of reconfigurable trimers. (*A*) Schematic showing the filling of the 3D-traps with sCAPA for a single colloidal 120-cluster. The numbers indicate the order of the deposition steps and the arrows respective deposition directions. (*B*–*D*) Combined bright-field+fluorescence micrographs of R-G-PS trimers in the sCAPA traps with 60 (*B*), 120 (*C*), and 180 (*D*) degrees between the microgels. Scale bars are 5 μm.

Three-State Dynamics of 120-Clusters: an Example. We first focus on the dynamical response of the 120-clusters as an example and later move on to a general description of all cases. After assembly and harvesting, the trimers are inserted in the same experimental cell that we previously described for the dumbbells and the transverse AC electric field (7 V peak-to-peak at 800 Hz) is applied together with light illumination of varying power density I at 395 nm to induce the local heating (Fig. 4*A*). In particular, we use a sequence of illumination/heating steps in the following order: 30 s no illumination (≈ 21 °C), 60 s at 33 mW mm^{-2} (≈ 31°C), 30 s at 92 mW mm^{-2} (≈ 45 °C), and finally 60 s no illumination (Fig. 4*B*). This sequence enables us to switch between a state where both microgels are swollen (GR), one where one microgel is swollen and the other one is collapsed (G'R), one where both microgels are collapsed (G'R'), and back to the initial state where both microgels are swollen again (GR) (Fig. 4*B*). We observe rapid and reversible switching amongst the various states, which is reflected in a qualitative and quantitative variation of the trajectories (Fig. 4*C*): in state (GR), the trajectory is chiral with a constant radius; in (G'R), the particle continues with a strong chiral motion, but with larger fluctuations and a higher velocity; and, finally, in (G'R'), the propulsion velocity drops and the rotational diffusivity of the cluster increases, resulting in noisier nonchiral motion. Upon removal of fluorescence illumination, the trajectory resumes the original characteristics of state (GR) (*SI Appendix*, Movie S1). By quantitatively tracking the motion of the trimers as a function of time/illumination, we further characterize their motility in terms of their self-propulsion velocity and rotational diffusion.

The trajectory reported in Fig. 4*C* corresponds to the experimental particle whose behavior most closely matches the median behavior of all analyzed 120-clusters across the three states, in terms of their net swimming velocity and rotational diffusivity (Fig. 4*D*). The trajectory can be rationalized by considering the direction of the propulsive force and of viscous drag, together with the cluster's rotational dynamics. As we have previously discussed in Fig. 1, in the case of dumbbells, propulsion is aligned with the direction of compositional asymmetry, and as a consequence of geometry, the center of propulsion and of hydrodynamic drag coincide. However, this is not necessarily the case for the trimers. As schematically shown in *SI Appendix*, Fig. S15 (*SI Appendix*, section 6), we can rationalize the propulsion of the trimer as the linear superposition of the propulsion generated by two dumbbells, respectively, connecting the PS particles to the G and the R microgels. Differences in the magnitude of each velocity vector and of the size of the respective dumbbell lobes may cause a

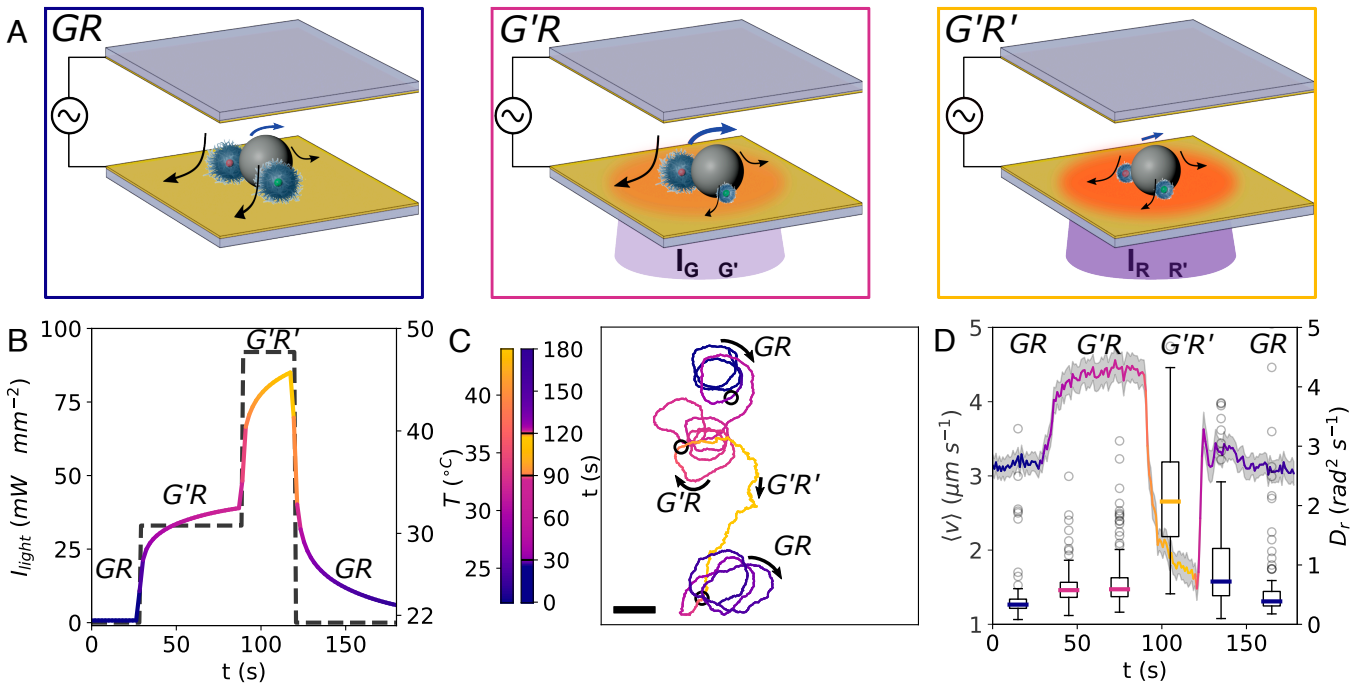

Fig. 4. Three-state dynamics for G-R-PS 120-clusters. (*A*) Schematic illustrating the 120-cluster in state *GR*, *G'R*, or*G'R'* depending on the illumination conditions. The black arrows represent the EHDFs and the blue ones indicate net propulsion. (*B*) Light exposure sequence (dashed line) over time and resulting temperatures (solid line) as predicted by finite element simulations. The color coding of the temperature corresponds to the color scale bar on the right of the graph. (*C*) Example trajectory of a G-R-PS 120-cluster color-coded with time and corresponding temperature as represented by the color scale bars on the left of the graph. This trajectory displays the closest resemblance to the average behavior of the whole data set. The scale bar is 20 μm. (*D*) Mean self-propulsion velocity (solid line) and rotational diffusion (box plots) of the microswimmers over time color-coded with temperature. The shaded bands are the 99% confidence intervals for the velocity calculated over between 100 to 124 trajectories. In the box plot, the colored line indicates the median, the size of the box indicates the interquartile range (IQR), and the whiskers delimit the range (Q1-1.5*IQR)–(Q3+1.5*IQR), where Q1 and Q3 delimit the first and third quartile of the data, and the dots mark the outliers.

misalignment between the center of propulsion and the center of hydrodynamic drag, giving rise to a rotation-translation coupling and the corresponding emergence of an active torque (39–42). With this simple image in mind, and considering the temperature response of the individual G-PS and R-PS self-propelled dumbbells, we can explain the multistate dynamics of the 120-cluster, as shown in Fig. 4 *C* and *D*. In state (GR), each microgel has a similar size and generates similar EHDFs. However, these are not identical, leading to a breaking of the in-plane symmetry of the trimer's propulsion and drag, which results in a chiral trajectory. In (G'R), the G-microgel collapses with a drop of the G-PS propulsion velocity and of the associated hydrodynamic drag, while the propulsion velocity of the R-microgel increases slightly. The reduced drag combined with increased temperature further leads to a slight but measurable increase in the rotational diffusivity, resulting in a less deterministic trajectory. Finally, in (G'R'), both microgels are collapsed and provide a significantly lower propulsive force. Correspondingly, the trimer's velocity drops and, combined with the overall decreased size of the microswimmer, leads to a significantly higher rotational diffusivity. The increased rotational diffusivity results in a nonchiral trajectory in state (G'R') that is well-described by the standard active Brownian particle ABP model, as we will show in the next section.

Analysis of Multistate Dynamics. After discussing a specific example, and in order to have a broader description of the dynamical states accessible to the clusters, we performed a statistical analysis of chirality, net swimming velocity, and mean-squared displacements of the whole population of 60-, 120-, or 180-clusters, to systematically classify their motion in the different states (Fig. 5).

First, we investigate the chirality of the trajectories in more detail. As previously stated, chiral trajectories result from breaking the in-plane symmetry of the propulsion and drag of the trimers. Even if sCAPA yields a narrow distribution of opening angles between the central PS particle and the two microgels, the two populations of microgels have an inherent difference in size and dielectric properties, as well as an intrinsic polydispersity, which can subtly change the asymmetry of each individual cluster and the chirality of its trajectory. To better understand the variation within each population, we extract the angular velocity and rotational diffusivity using the distributions of angular displacements for all particles (*SI Appendix*, section 7 for details). We consider two categories: chiral particles with clockwise (CW) or counter-clockwise (CCW) rotation, and nonchiral particles that we refer to as generic Active Brownian Particles (ABPs). We define that a trajectory cannot be classified as statistically chiral if the observed mean angular displacement falls within the SD of the distribution of random angular displacements resulting from rotational diffusivity. This criterion identifies the fraction of clusters with chiral motion for the different opening angles and states, as shown in Fig. 5*B*.

As seen in the data, the 60-clusters (*SI Appendix*, Movie S2) have the largest self-propulsion velocity in state (GR) (Fig. 5*C*), where approximately 50% of them have chiral trajectories, with an angular velocity between 0.33 and 0.72 rad s^{-1} (*SI Appendix*, section 8). However, unlike the 120- and 180-clusters, their velocity drops already in (G'R) and remains similar in (G'R'), alongside an almost total suppression of chiral motion. We

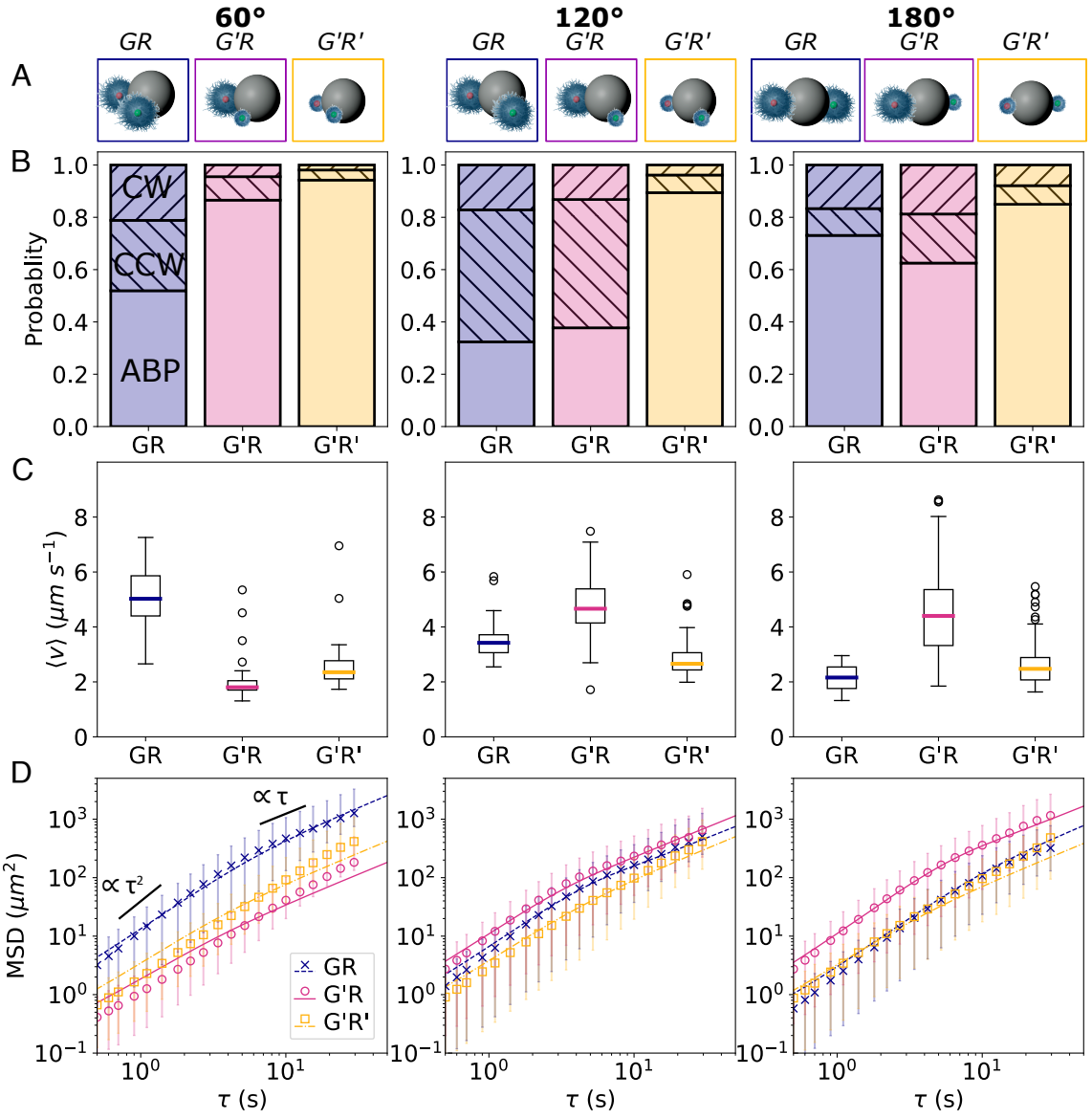

Fig. 5. Multistate motility of different active clusters. Each column corresponds to the 60-, 120- or 180-clusters, respectively. (*A*) Schematic of the three clusters in state (GR),(G'R), and (G'R'). (*B*) Fraction of trajectories that display clockwise chiral motion (CW, right-leaning dashes), counter-clockwise chiral motion (CCW, left-leaning dashes), or nonchiral active Brownian particle motion (ABP, no dashes) in (GR), (G'R), and (G'R'). The criterion for chiral motion is $\langle|\omega|\rangle t > 2 * \sqrt{D_r t}$ for t = 30 s. (*C*) Box plot of the mean self-propulsion velocity in (GR), (G'R), or (G'R'). The box plots are calculated from between 52 to 79, 106 to 104, and 78 to 144 trajectories for the 60-, 120- or 180-clusters, respectively. In the box plot, the colored line indicates the median, the size of the box indicates the interquartile range (IQR), and the whiskers delimit the range (Q1-1.5*IQR)–(Q3+1.5*IQR), where Q1 and Q3 delimit the first and third quartile of the data, and the dots mark the outliers. (*D*) Ensemble-averaged MSD in (GR), (G'R), or (G'R'). Symbols: experimental data. Lines: computed MSD of for a chiral active Brownian particle with the $\langle|\omega|\rangle$, $\langle v\rangle$, and $\langle D_r\rangle$ of each state (43).

hypothesize that this response is due to the fact that, at a 60-degree opening angle, the two microgels substantially overlap in the swollen state such that the collapse of the G microgel already causes the shirking of the R microgel, practically eliminating any difference between (G'R) and (G'R') (*SI Appendix*, section 10 for further details).

Conversely, the largest chiral fraction in state *(GR)* is observed for the 120-clusters, which is reflected in the shape of the median trajectory previously described in Fig. 4*C*. Between state (GR) and (G'R), the fraction of chiral trajectories remains similar, and due to the collapse of the G microgel combined with a small increase in the R-PS EHDF velocity, their angular velocity slightly increases from between 0.23 and 1.05 rad s^{-1} to 0.32 and 1.2 rad s^{-1} (*SI Appendix*, section 8 and more details on the transitions between these states are found in *SI Appendix*, section 9). We then observed a nearly complete loss of chirality in state (G'R'), as the fraction of particles meeting our criterion drops as a function of the overall reduction of propulsion velocity and increase of rotational diffusivity.

The 180-clusters (*SI Appendix*, Movie S3) conversely have a low self-propulsion velocity in state (GR) (Fig. 5*C*) and less than 30% of chiral clusters with an angular velocity between 0.28 and 0.82 rad s^{-1} (*SI Appendix*, section 8). However, the transition to state (G'R) shows a much more significant speeding up combined with a slight increase in the chirality, while in state (G'R') the behavior is very similar to one of the 60- and 120-clusters. Moreover, similarly to the 120-clusters, the median trajectories of the 180-clusters can be rationalized by the EHDF

vector model introduced in the previous section and described in *SI Appendix*, section 6. In state (GR), the propulsive forces of the 2 microgel-PS dumbbells are similar in magnitude but oppose each other leading to a small net propulsion. Switching to (G'R) breaks this balance, the G microgel collapses, and the clusters speed up. Slight misalignment of the microgels can explain the increase in chiral motion in some of the 180-clusters.

This systematic analysis shows that the different transitions affect the reconfiguration and the motility of the various clusters differently, in ways that could not be simply achieved by rigid units with varying velocities. As a consequence, the way in which our adaptive microswimmers explore space, which can be represented by plotting their ensemble-averaged mean-square displacements (MSDs), becomes a function of their geometry and internal state. The ensemble-averaged MSDs of the total populations reported in Fig. 5*D* are in good agreement with the predicted MSDs for swimmers with the corresponding median properties ($< v >$, ω and D_R) (43). The 60- and 180-clusters have a clear state in which they spread out fastest, which is (GR) for the 60-clusters and (G'R) for 180-clusters, respectively. These states correspond to high self-propulsion velocities and small angular velocities/rotational diffusivities, for which space is explored significantly faster than in the lower-velocity states at all times. The MSD for 120-clusters is more nuanced, with the mean-squared displacement of the different states varying less compared to the 60- and 180-clusters despite similar differences in swimming velocities. The ensemble MSD of chiral swimmers with monodisperse angular velocities and low rotational diffusivity has a characteristic sinusoidal shape as the trajectories loop back on themselves (43). However, in our ensemble average, this feature is washed out by superimposing the displacements of particles with a broad range of angular velocities and including nonchiral trajectories (ABPs). However, the overall chiral motion still results in lower MSD than expected for nonchiral ABPs with the same velocity and rotational diffusivity (*SI Appendix*, section 11 for separated chiral and nonchiral MSDs). Although specific differences are averaged out by examining a heterogeneous population, the ensemble data are representative of the average dynamical behavior of each geometry.

Conclusions and Outlook. In this manuscript, we have incorporated stimuli-responsive microgels into deterministically assembled colloidal clusters using sCAPA, resulting in synthetic microswimmers with distinct internal states coupled to their dynamical modes. Importantly, and differently from typical light-driven or magnetically driven particles, where the stimuli for propulsion and the ones that regulate motility coincide (44–46), our system relies on orthogonal propulsion and reconfiguration mechanisms (21). Our strategy can thus be extended to implement spatially and temporally modulated motility landscapes to investigate collective effects, in analogy with light-regulated swimming bacteria (47, 48).

Our findings further suggest potential future applications, where reconfiguration and single-particle control can be used in lab-on-chip devices. The AC-electrodes can be integrated into microfluidic systems where reconfigurable microswimmers can navigate based on thermal signals. We envision that 60-clusters could, for instance, explore space efficiently and linger in high-temperature regions delivering reagents for chemical reactions, while 180-clusters could remove reaction products and transfer them to colder regions, due to their different dynamical responses. Even though thermal signaling may not be practical for all applications, incorporating responses to different stimuli will provide further options.

In fact, the modular assembly enabled by sCAPA makes it possible to incorporate other soft components, which can reconfigure in response to different stimuli. PNIPAM-based microgels that are responsive to light (49), pH (33, 34), redox state (50), magnetic fields (51), and (bio)chemical molecules (52) have been synthesized. The use of multiple orthogonal stimuli would greatly increase the number of possible states, compared to using only one stimulus, e.g., temperature, with different transitions.

Finally, in order to successfully assemble precisely programmed reconfigurable clusters, we had to challenge sCAPA beyond the state of the art with the introduction of 3D height profiles within the traps to direct the deposition of soft and hard particles in deterministic shapes. In the future, we also envisage that additional strategies can be used to incorporate reconfigurable parts in microscale active units. Achieving microgel populations with more narrowly distributed properties and improving microfabrication techniques could reduce the variations in the dynamical responses, improving the overall control over different states and in particular encoding specific chirality. Recent advances in 3D-printing of microscale responsive hydrogels with two-photon nanolithography could allow for a more flexible fabrication of soft structures (53), toward hybrid active colloidal materials (37, 54).

All of these efforts are ultimately motivated to push the boundaries of our current capabilities to endow microscale systems with elements of physical intelligence and will take a very active community of researchers and engineers one step, or more, closer to the goal of realizing autonomous microscale systems with capabilities mirroring the ones of larger-scale robotic units.

Materials and Methods

All chemicals, if not stated otherwise, were used as provided by the supplier. Triton X-45, acrylic acid (AA), methacrylic acid (MAA), N, N′ methylenebis(acrylamide) (BIS), 2,2,2-trifluoroethyl methacrylate (TFMA), sodium dodecyl sulfate (SDS), potassium persulfate (KPS), BODIPY, and Nile red were purchased from Sigma-Aldrich. N-Isopropylacrylamide (NIPAM) was purchased from Sigma-Aldrich and purified by recrystallization in Toluene/Hexane 50:50. 4-(2-hydroxyethyl)-1-piperazineethanesulfonic acid (HEPES) was purchased from VWR.

Synthesis of Core-Shell pNIPAM Microgels. The microgels with fluorescent cores and thermoresponsive shells were prepared in a two-step synthesis (55): First, the PTFMA-cores containing fluorescent dyes were prepared using free-radical emulsion polymerization, then a shell of PNIPAM and PAA or PMAA copolymer was grown by free-radical precipitation polymerization around this core. For the cores, TFMA (10 mL; 12 g; 70,3 mmol), NIPAM (940 mg; 8,31 mmol), SDS (30 mg; 0,104 mmol), and Nile red (5 mg; 0.016 mmol) or BODIPY 493/503 (5 mg; 0,016 mmol) were added in water (30 mL) and stirred at 600 rpm for 20 min and purged with N_2. The reaction mixture was heated up to 70 °C. KPS (25 mg; 0.093 mmol), previously dissolved in water (2.5 mL), was added after the emulsion was stirred for 15 min at 70 ° C. After 4 h of stirring at 70 °C, the reaction was stopped by contact with air. The resulting particles were directly filtered. The purification of the particles was carried out via centrifugation followed by decantation, the addition of Milli-Q water, and particle redispersion. The purification via centrifugation was performed three times. To remove SDS residues, the redispersed particles were dialysed in water for 24 to 72 h (dialysis tube membrane: 12 to 14 kDa). The particles were analyzed with dynamic light scattering (ZetaSizer Nano DLS).

The PNIPAM-co-AA / PNIPAM-co-MAA shells were grown by first dissolving NIPAM(1.15g), BIS(11.5 mg) and MAA or AA(88.5 μl) in 50 ml milli-Q water. Then, 300 μl of the core particle suspension was added. The mixture was stirred at 600 rpm for 20 min and purged with N_2. The reaction mixture was heated up to 70 ° C and KPS (25 mg; 0.093 mmol) was slowly added. After 2 h, the reaction reached completion and the microgel suspension was filtered and dialysed for 48 h (dialysis tube membrane: 12 to 14 kDa). The particles were characterized with DLS.

Fabrication of Colloidal Molecules. The responsive microswimmers were prepared using sequential capillarity-assisted particle assembly (sCAPA). The basic principles of sCAPA are described by Ni et al. (22). Here, we used an adapted version of sCAPA, which uses masters prepared with direct writing via two-photon nanolithography, as opposed to Si masters made with conventional lithography methods. Briefly, negative masters were prepared with two-photon lithography (Nanoscribe Photonic Professional GT2) using a 63x oil-immersion objective and IP-Dip solution set (37). The masters contained 6 smaller areas with 10,000 "traps" each, and one area was used to prepare the particles for one experiment. After printing and developing under standard conditions, these masters were postcured for 2 h under a UV-lamp and coated with a perfluoro silane using chemical vapor deposition. PDMS (Sylgard 184) was used to make templates from these masters. sCAPA was performed as described in the following paper (38). The PS particles were deposited from a 0.035% Triton X-45 and 3.5 mM SDS solution in Milli-Q water. The microgels were from a 0.04% Triton X-45 in 1 mM HEPES pH 7.4 or 0.025% Triton X-45 in 1 mM MES pH 4.5 for green- and red-core microgels, respectively. All depositions were carried out at 25 °C with a deposition rate of 3 μm s^{-1}.

Active Motion Experiments. The colloidal clusters were activated using AC electric fields in a closed cell with the top and bottom electrodes consisting of transparent conductive slides separated by a 240-μm-thick spacer (Grace Bio-Labs SecureSeal, USA, custom shape). The conductive slides were borosilicate microscope slides coated with 3 nm Cr and 10 nm Au by thermal evaporation. The bottom slide on which the particles move was treated with thiolated polyethylene glycol (6 kDA, 1 mM in Milli-Q water, 30 min) to prevent sticking. The colloidal molecules were transferred from the sCAPA-templates to the top electrode, previously coated by a 3-μm-thick spin-coated layer of glucose (40% wt. in DI-water, 30 s 4,000 rpm). Upon exposing the top slide to the suspending medium (0.1 mM HEPES buffer at pH 7 and 0.001% wt. Triton in Milli-Q water) and closing the cell, the glucose layer dissolved and the particles sedimented to the bottom electrode. The conductive slides were connected to a function generator (Agilent 33500B) with copper leads made from 50 μm copper foil, and the experiments were performed on an Eclipse Nikon Ti2-e with a Lumencor Spectra II lightbox and a 20x objective. The particles were actuated by applying an AC field with 800 Hz frequency and 7 V peak-to-peak amplitude. The field was applied for 15 min to equilibrate the sample before collecting data. Movies were recorded in a 1024 * 1024 px^2 window (340 * 340 μm^2) at 10 frames per second. The local temperature was regulated through illumination with the 395-nm and 555-nm light sources of the lightbox (*SI Appendix* for more details).

All the particles in the field of view were located and tracked using the TrackPy library in Python (56). Stuck particles and particles that got stuck during the experiment were omitted from the analysis. The self-propulsion velocity of every individual particle was determined by measuring their displacements over 0.5 s windows (5 frames). The chirality and rotational diffusion were determined by investigating the distribution of angular displacements at different lag times in 30-s windows (*SI Appendix*, section 7 for more details), corresponding to the time windows over which temperature was changed.

Data, Materials, and Software Availability. All study data are included in the article and/or *SI Appendix*. All the data and codes have been deposited in the following publicly accessible database https://doi.org/10.3929/ethz-b-000598257.

ACKNOWLEDGMENTS. L.A. acknowledges the financial support from the European Soft Matter Infrastructure (EUSMI) proposal number S180600105. This project has received funding from the European Research Council (ERC) under the European Union's Horizon 2020 research and innovation program grant agreement No. 101001514. We thank Alexander Kuehne and Dirk Rommels for their help with particle synthesis and discussion.

Author affiliations: [a]Laboratory for Soft Materials and Interfaces, Department of Materials, ETH Zurich, Zurich, Switzerland; [b]CNRS, Univ. Bordeaux, CRPP, UMR5031, Pessac 33600, France; and [c]Centro de Física de Materiales (SCIC-UPV/EHU), Materials Physics Center, San Sébastian 20018, Spain

1. M. Sitti, Physical intelligence as a new paradigm. *Extreme Mech. Lett.* **46**, 101340 (2021).
2. R. L. Truby, Designing soft robots as robotic materials. *Acc. Mater. Res.* **2**, 854–857 (2021).
3. S. Felton, M. Tolley, E. Demaine, D. Rus, R. Wood, A method for building self-folding machines. *Science* **345**, 644–646 (2014).
4. K. Y. Ma, P. Chirarattananon, S. B. Fuller, R. J. Wood, Controlled flight of a biologically inspired, insect-scale robot. *Science* **340**, 603–607 (2013).
5. W. Hu, G. Z. Lum, M. Mastrangeli, M. Sitti, Small-scale soft-bodied robot with multimodal locomotion. *Nature* **554**, 81–85 (2018).
6. C. Krüger, G. Klös, C. Bahr, C. C. Maass, Curling liquid crystal microswimmers: A cascade of spontaneous symmetry breaking. *Phys. Rev. Lett.* **117**, 048003 (2016).
7. F. Lancia *et al.*, Reorientation behavior in the helical motility of light-responsive spiral droplets. *Nat. Commun.* **10**, 5238 (2019).
8. B. E. F. De Ávila *et al.*, Micromotor-enabled active drug delivery for in vivo treatment of stomach infection. *Nat. Commun.* **8**, 1–8 (2017).
9. A. C. Hortelao *et al.*, Swarming behavior and in vivo monitoring of enzymatic nanomotors within the bladder. *Sci. Rob.* **6**, eabd2823 (2021).
10. M. B. Akolpoglu *et al.*, Magnetically steerable bacterial microrobots moving in 3d biological matrices for stimuli-responsive cargo delivery. *Sci. Adv.* **8**, 6163 (2022).
11. V. Sridhar *et al.*, Light-driven carbon nitride microswimmers with propulsion in biological and ionic media and responsive on-demand drug delivery. *Sci. Robot* **7**, 1421 (2022).
12. S. Schuerle *et al.*, Synthetic and living micropropellers for convection-enhanced nanoparticle transport. *Sci. Adv.* **5** (2019).
13. H. Wang, B. Khezri, M. Pumera, Catalytic DNA-functionalized self-propelled micromachines for environmental remediation. *Chem* **1**, 473–481 (2016).
14. R. Wang *et al.*, Highly efficient MOF-based self-propelled micromotors for water purification. *RSC Adv.* **7**, 42462–42467 (2017).
15. Y. Dou, K. J. M. Bishop, Autonomous navigation of shape-shifting microswimmers. *Phys. Rev. Res.* **1**, 032030 (2019).
16. S. Ni, E. Marini, I. Buttinoni, H. Wolf, L. Isa, Hybrid colloidal microswimmers through sequential capillary assembly. *Soft Matter* **13**, 4252–4259 (2017).
17. Z. Wang *et al.*, Active patchy colloids with shape-tunable dynamics. *J. Am. Chem. Soc.* **141**, 14853–14863 (2019).
18. R. Soto, R. Golestanian, Self-assembly of catalytically active colloidal molecules: Tailoring activity through surface chemistry. *Phys. Rev. Lett.* **112**, 068301 (2014).
19. R. Niu, T. Palberg, T. Speck, Self-assembly of colloidal molecules due to self-generated flow. *Phys. Rev. Lett.* **119**, 028001 (2017).
20. H. Lowen, Active colloidal molecules. *Eur. Lett.* **121**, 58001 (2018).
21. L. Alvarez *et al.*, Reconfigurable artificial microswimmers with internal feedback. *Nat. Commun.* **12** (2021).
22. S. Ni, J. Leemann, I. Buttinoni, L. Isa, H. Wolf, Programmable colloidal molecules from sequential capillarity-assisted particle assembly. *Sci. Adv.* **2**, e1501779–e1501779 (2016).
23. W. D. Ristenpart, I. A. Aksay, D. A. Saville, Electrohydrodynamic flow around a colloidal particle near an electrode with an oscillating potential. *J. Fluid Mech.* **575**, 83–109 (2007).
24. F. Ma, X. Yang, H. Zhao, N. Wu, Inducing propulsion of colloidal dimers by breaking the symmetry in electrohydrodynamic flow. *Phys. Rev. Lett.* **115** (2015).
25. F. Ma, S. Wang, D. T. Wu, N. Wu, Electric-field-induced assembly and propulsion of chiral colloidal clusters. *Proc. Natl. Acad. Sci. U.S.A.* **112**, 6307–6312 (2015).
26. C. W. Shields, O. D. Velev, The evolution of active particles: Toward externally powered self-propelling and self-reconfiguring particle systems. *Chem* **3**, 539–559 (2017).
27. W. Su, K. Zhao, J. Wei, T. Ngai, Dielectric relaxations of poly(n-isopropylacrylamide) microgels near the volume phase transition temperature: Impact of cross-linking density distribution on the volume phase transition. *Soft Matter* **10**, 8711–8723 (2014).
28. P. S. Mohanty *et al.*, Dielectric spectroscopy of ionic microgel suspensions. *Soft Matter* **12**, 9705–9727 (2016).
29. A. Fernández-Nieves, A. Fernández-Barbero, B. Vincent, F. J. D. L. Nieves, Charge controlled swelling of microgel particles. *Macromolecules* **33**, 2114–2118 (2000).
30. A. Ruscito *et al.*, Microgel particles with distinct morphologies and common chemical compositions: A unified description of the responsivity to temperature and osmotic stress. *Gels* **6**, 1–19 (2020).
31. C. Scherzinger, A. Schwarz, A. Bardow, K. Leonhard, W. Richtering, Cononsolvency of poly-N-isopropyl acrylamide (PNIPAM): Microgels versus linear chains and macrogels. *Curr. Opin. Colloid Interface Sci.* **19**, 84–94 (2014).
32. C. L. Lin, W. Y. Chiu, C. F. Lee, Preparation, morphology, and thermoresponsive properties of poly(n-isopropylacrylamide)-based copolymer microgels. *J. Polymer Sci. Part A: Polymer Chem.* **44**, 356–370 (2006).

33. K. Kratz, T. Hellweg, W. Eimer, Influence of charge density on the swelling of colloidal poly(n-isopropylacrylamide-co-acrylic acid) microgels. *Colloids Surf. A: Physicochem. Eng. Aspects* **170** (2000).
34. X. Gao *et al*., PH- and thermo-responsive poly(N-isopropylacrylamide-co-acrylic acid derivative) copolymers and hydrogels with LCST dependent on pH and alkyl side groups. *J. Mater. Chem. B* **1**, 5578–5587 (2013).
35. J. H. Son *et al*., Ultrafast photonic PCR. *Light: Sci. Appl.* **4** (2015).
36. COMSOL AB, Comsol multiphysics® v. 5.5. (2020).
37. S. van Kesteren, X. Shen, M. Aldeghi, L. Isa, Printing on particles: Combining two-photon nanolithography and capillary assembly to fabricate multi-material microstructures. arXiv [Preprint] (2022). https://arxiv.org/10.48550/ARXIV.2208.02635.
38. S. Ni, J. Leemann, H. Wolf, L. Isa, Insights into mechanisms of capillary assembly. *Faraday Discuss.* **181**, 225–242 (2015).
39. H. Brenner, Coupling between the translational and rotational Brownian motions of rigid particles of arbitrary shape II. General theory. *J. Colloid Interface Sci.* **23**, 407–436 (1967).
40. A. Chakrabarty *et al*., Brownian motion of arbitrarily shaped particles in two dimensions. *Langmuir* **30**, 13844–13853 (2014).
41. Z. T. Zhang, X. Zhao, B. Y. Cao, Diffusion tensors of arbitrary-shaped nanoparticles in fluid by molecular dynamics simulation. *Sci. Rep.* **9** (2019).
42. D. J. Kraft *et al*., Brownian motion and the hydrodynamic friction tensor for colloidal particles of complex shape. *Phys. Rev. E - Stat. Nonlinear Soft Matter Phys.* **88** (2013).
43. R. J. Archer, A. I. Campbell, S. J. Ebbens, Glancing angle metal evaporation synthesis of catalytic swimming Janus colloids with well defined angular velocity. *Soft Matter* **11**, 6872–6880 (2015).
44. K. Han *et al*., Sequence-encoded colloidal origami and microbot assemblies from patchy magnetic cubes. *Sci. Adv.* **3**, 1–7 (2017).
45. C. Lozano, B. Ten Hagen, H. Löwen, C. Bechinger, Phototaxis of synthetic microswimmers in optical landscapes. *Nat. Commun.* **7**, 12828 (2016).
46. C. Lozano, C. Bechinger, Diffusing wave paradox of phototactic particles in traveling light pulses. *Nat. Commun.* **10**, 2495 (2019).
47. J. Arlt, V. A. Martinez, A. Dawson, T. Pilizota, W. C. Poon, Painting with light-powered bacteria. *Nat. Commun.* **9**, 768 (2018).
48. G. Frangipane *et al*., Dynamic density shaping of photokinetic *E. coli*. *eLife* **7**, 1–14 (2018).
49. M. Das, N. Sanson, D. Fava, E. Kumacheva, Microgels loaded with gold nanorods: Photothermally triggered volume transitions under physiological conditions. *Langmuir* **23**, 196–201 (2007).
50. D. Suzuki, R. Yoshida, Temporal control of self-oscillation for microgels by cross-linking network structure temporal control of self-oscillation for microgels by cross-linking network structure. *Sci. Technol.* 5830–5838 (2008).
51. S. Rittikulsittichai *et al*., Multi-responsive hybrid particles: Thermo-, pH-, photo-, and magneto-responsive magnetic hydrogel cores with gold nanorod optical triggers. *Nanoscale* **8**, 11851–11861 (2016).
52. Z. Tang, Y. Guan, Y. Zhang, Contraction-type glucose-sensitive microgel functionalized with a 2-substituted phenylboronic acid ligand. *Polymer Chem.* **5**, 1782–1790 (2014).
53. M. Hippler *et al*., Controlling the shape of 3D microstructures by temperature and light. *Nat. Commun.* **10** (2019).
54. X. Hu *et al*., Magnetic soft micromachines made of linked microactuator networks. *Sci. Adv.* **7** (2021).
55. D. Go, T. E. Kodger, J. Sprakel, A. J. Kuehne, Programmable co-assembly of oppositely charged microgels. *Soft Matter* **10**, 8060–8065 (2014).
56. D. B. Allan, T. Caswell, N. C. Keim, C. M. van der Wel, R. W. Verweij, soft-matter/trackpy: Trackpy v0.5.0 (2021).